

# Microbenchmarking NVIDIA’s Blackwell Architecture: An in-depth Architectural Analysis

Aaron Jarmusch

dept. of Computer Information Sciences  
University of Delaware  
Newark, US

Sunita Chandrasekaran

dept. of Computer Information Sciences  
University of Delaware  
Newark, US  
schandra@udel.edu

*Abstract—*

As GPU architectures rapidly evolve to meet the overcoming demands of exascale computing and machine learning, the performance implications of architectural innovations remain poorly understood across diverse workloads. NVIDIA’s Blackwell (B200) generation introduce significant architectural advances including the 5th generation tensor cores, tensor memory (TMEM), decompression engine (DE), and dual chips; however systematic methodologies for quantifying these improvements lag behind hardware development cycles. We contribute an open-source microbenchmark suite that offers practical insights into optimizing workloads to fully utilize the rich feature sets of the modern GPU architecture. This work aims to enable application developers make informed architectural decisions and guide future GPU design directions.

Our work studies Blackwell GPUs, compares them to H200 generation with regards to the memory subsystem, tensor core pipeline and floating-point precisions (FP32, FP16, FP8, FP6, FP4). Our systematic evaluation of dense/sparse GEMM, transformer inference, and training workloads demonstrate that B200’s tensor core enhancements achieves 1.56× higher mixed-precision throughput and 42% better energy efficiency than H200. Our memory analysis reveals 58% reduction in memory access latency in cache-misses, fundamentally changing optimal algorithm design strategies.

*Index Terms—*Blackwell, GPU, Microbenchmark, HPC

## I. INTRODUCTION

Artificial Intelligence (AI) and high-performance computing (HPC) have evolved into data-intensive disciplines that continuously challenge hardware efficiency, scalability, and precision. Large language models (LLMs) now exceed hundreds of billions of parameters and process context windows spanning millions of tokens [1], [2], alongside multi-physics and climate simulations that demand teraflops of sustained performance, thus shifting GPU design to enable both massive parallel and architectural adaptability. At these scales, modern accelerators must balance several demands: maintaining arithmetic throughput for dense tensor workloads, minimizing on-chip and off-chip memory latency, while offering hardware primitives that effectively support mixed-precision computation.

The growing demands have exposed several limitations of current GPU architectures, particularly within their memory hierarchies, precision flexibility, and latency-sensitive task scheduling. As a result, sustained architectural innovation in accelerators has become essential for advancing both throughput-optimized training and time-critical inference

workloads. One such architecture that is designed to address some of these challenges is NVIDIA’s Blackwell architecture [3] that showcases a major generational evolution.

As the direct successor to the Hopper generation, the Blackwell architecture extends NVIDIA’s GPU design in several modifications across the compute pipeline, memory hierarchy, and tensor processing subsystems. Blackwell introduces 5th-generation Tensor Cores capable of FP4 and FP6 precision execution, offering trade-offs between accuracy and performance for large-scale training. In addition, the introduction of the Tensor Memory (TMEM) subsystem as a dedicated on-chip memory for tensor data movement reduces reliance on shared memory (SMEM) and per SM register files (RF) during matrix-intensive operations. Next, NVIDIA included a hardware decompression engine (DE) and redesigned the instruction pipeline for access to compressed model weights. Beyond raw compute enhancements, Blackwell also has a revised thread and CTA scheduling model to utilize inter-SM communication and memory concurrency. With so many changes introduced, intended to address the escalating demands of AI, gaming and scientific computing, an analysis of the microarchitecture and new instructions is necessary, which will provide application developers and scientists to achieve the highest performance possible for modern and future GPUs.

This paper introduces a newly developed open-source microbenchmark suite (unable to share the code at this time due to double-blind), implemented in PTX and CUDA, that enables comprehensive architectural analysis of NVIDIA’s Blackwell GPU. Emphasizing innovations that distinguish it from Hopper, the suite systematically evaluates performance under stress—particularly in compute-bound and memory-bound workloads—revealing implications for parallel computing applications.

The key contributions of our work are as follows:

- Build targeted microbenchmarks to characterize key components of NVIDIA Blackwell B200, to the best of our knowledge - our work is the first detailed microbenchmark characterization of this next-generation GPU.
- Quantify TMEM’s impact on matrix-heavy workloads and its role in reducing memory bottlenecks in tensor computations.
- Evaluate the decompression engine’s throughput across formats and identify optimal usage.

- Analyze 5th-gen Tensor Core execution via the new `tcgen05` PTX instructions to study performance implications
- Assess FP4/FP6 performance and accuracy trade-offs in mixed-precision tensor operations quantifying accuracy-performance trade-offs
- Benchmark Blackwell across LLM inference/training, scientific kernels, and mixed-precision workloads to demonstrate real-world impact and performance gains.
- Provide actionable performance guidelines for developers leveraging Blackwell’s architecture.

The remainder of this paper is organized as follows: Section II details our contributions to the current state of the art GPU microbenchmarks. Following, Section III presents an overview of the Blackwell’s B200 architecture. After which, Section IV details the microbenchmark methodology we employ to systematically characterize the Blackwell microarchitecture. While, Section V details the memory subsystem before Section VI presents the Tensor Core pipeline. Section VII presents performance analysis across key workloads and to conclude we discuss implications and trade-offs in Section VIII.

## II. RELATED WORK

Understanding GPU performance has long been a critical focus in HPC research. Over the years, several studies have used microbenchmarks and other methodologies to dissect architectural layers and analyze GPU microarchitectures in fine-grained detail. Early studies on Tesla and Fermi focused on memory and cache behavior [4], [5], while later work dissecting Kepler, Pascal [6], and Maxwell [7] examined warp scheduling and instruction latency. With Turing through Hopper [8]–[15], research shifted to mixed-precision and tensor core performance, introducing benchmarks for `mma` instructions, tile sizes, and data layouts. Recent efforts also explore instruction-level parallelism [16], and pipeline dynamics under high register pressure.

Beyond microbenchmarking, researchers built frameworks to characterize GPU performance. Application profiling [17] gathers runtime metrics but faces overhead and limited architectural visibility. Roofline models [18] offer throughput vs. intensity plots, yet oversimplify bottlenecks and miss dynamic memory behaviors. Cache stall prediction [19] estimates pipeline delays from access patterns but fails to capture modern GPU complexities like cache bypassing, warp scheduling, and memory coalescing.

Analytical models like Accel-Sim [20] and GCoM [21], built on Hong and Kim’s work [22], offer useful GPU performance insights but neither of them model Blackwell-specific features like TMEM or the DE, as the detailed architectural information required for accurate simulation remain unknown.

Thus, without a systematic understanding of these components, the research community lacks critical data needed for performance modeling, workload optimization, and accurate simulation of AI reasoning workloads typically needed for datacenter deployments.

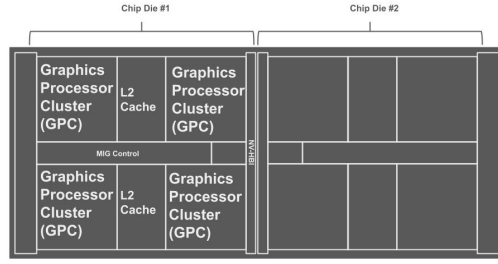


Fig. 1. NVIDIA Blackwell GPU dual-die design interconnected via NV-HBI.

## III. BLACKWELL ARCHITECTURE

In this Section, we introduce the architecture of the data center NVIDIA B200 GPU, based on the NVIDIA Blackwell Architecture, and then detail the divergence from prior designs.

### A. Blackwell Architecture

The B200 GPU signifies a decisive progression in architectural philosophy. Previously, GPU generations from Tesla to Hopper focused on maximizing floating-point operations per second (FLOPS) for large-scale model training. In contrast, Blackwell emphasizes post-training and inference efficiency, adopting transformational changes in both memory and compute organization. One B200 GPU includes a **dual-die configuration** [3] where two GPU dies comprise 208 billion transistors, feature 148 SMs spread across eight GPCs, provide four L2 cache partitions (double those in Hopper), and include eight HBM3e memory stacks. Though physically partitioned, both dies are unified by the NVIDIA High-Bandwidth Interface (NV-HBI) providing a coherent and single device to software, with unified 192 GB HBM3e memory space.

Within each SM, Blackwell introduces **fifth-generation Tensor Cores** that break from the warp-synchronous paradigm characterizing earlier architectures (Volta, Ampere, Hopper). Previous generations enforced that all 32 threads within a warp synchronize before executing matrix multiply–accumulate (MMA) operations via the `mma.sync` or `wgmma` instructions. This lock-step model reduced scheduling flexibility and created idle cycles, especially for dependency chains of varying lengths.

Blackwell replaces warp-synchronous MMA with `tcgen05.mma`, a single-thread instruction. Now, each thread independently issues MMA operations, removing warp-level synchronization and enabling true per-thread scheduling for tensor operations. Operands are now supplied from shared memory (SMEM) and a new memory pathway: **Tensor Memory (TMEM)**. Per SM, the TMEM provides memory access to and from tensor cores. Allocation, data movement, and deallocation are explicitly managed in software via the `tcgen` PTX set of instructions, giving compiler toolchains precise control over tile locality and traffic patterns.

The flexibility of independent MMA dispatch reduces idle cycles and exposes optimization opportunities for the compiler,

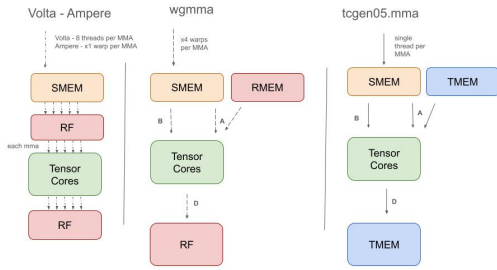


Fig. 2. Tensor Core instruction pipeline for `tcgen05`, `wgmma`, and Volta/Ampere architectures.

though it also raises questions on new performance limits: instruction latency under dependency, concurrency of tensor core usage, and pipeline saturation. These remain undocumented in vendor literature and are explored in our systematic characterization.

In terms of numerical support, Blackwell’s Tensor Cores introduce native **4-bit and 6-bit floating-point precision (FP4 and FP6)** for quantized inference, further improving memory and computational efficiency for AI workloads. Architectural innovations extend to the thread-block level, with **CTA pair execution**: two Cooperative Thread Arrays (CTAs) with adjacent ranks share operands, reducing redundant data movement. Each CTA pair maps to a TPC and leverages a dedicated intra-TPC communication network for efficient operand sharing.

Further broadening the functionality, Blackwell’s Tensor Cores provide native support for convolution operators with weight-stationary dataflows that use a collector buffer to cache and reuse matrix B (weight tensor) operands. Hence, optimizing for convolutional kernels that benefit from operand locality. Blackwell also addresses growing model and data sizes by introducing a hardware-based **Decompression Engine (DE)** to offload decompression tasks from general-purpose SMs. This subsystem supports various algorithms, more on that in Section V, enabling model weights and large database tables to be stored in compressed form within HBM3e and decompressed transparently during memory access [3].

While some architectural details are publicly disclosed, critical microarchitectural information, such as instruction latency, pipeline depth, cache interaction, and saturation, remains unknown. Our PTX microbenchmark experiments (Sections V-VI) provide a systematic investigation to fill these knowledge gaps as they relate to AI and HPC performance.

#### IV. PTX-MICROBENCHMARK METHODOLOGY

We employ a microbenchmarking approach based on NVIDIA’s Parallel Thread Execution (PTX) to characterize Blackwell’s microarchitectural features. While prior GPU characterization studies [4], [7], [14] established foundational PTX-level benchmarking principles, we extend these methodologies with novel techniques specifically designed to dissect Blackwell’s previously uncharacterized components, including the 5th-generation Tensor Cores’s FP4/FP6 precision modes, the DE, and the revised cache hierarchy.

Our approach leverages PTX to provide explicit control over registers and memory operations specific to architectures. PTX code is compiled into Streaming Assembler (SASS) instructions or machine code executed by the GPU. We ensure our microbenchmarks accurately isolate and measure specific microarchitectural behaviors by documenting the PTX-to-SASS translation and validating against observed performance.

##### A. Novel Benchmark Design for Blackwell-Specific Features

1) **Tensor Memory (TMEM)**: Unlike previous architectures where MMA operations relied exclusively on SMEM, DSMEM, and RFs, Blackwell introduces TMEM as a dedicated on-chip memory specifically for tensor operations. This necessitates new data movement paradigms and presents unexplored opportunities for performance optimization. Understanding TMEM’s performance characteristics is critical for several reasons. First, traditional data movement instructions (including `wmma.load`, `ldmatrix`, `ld.shared`, and `cp.async`) which cannot interface with TMEM. Thus developers are required to adopt entirely new instruction sequences (`tcgen05.ld`, `tcgen05.st`, `tcgen05.cp`). Second, the performance implications of this new memory tier remain uncharacterized, leaving application developers without guidance on when and how to leverage TMEM effectively.

Our work addresses this gap by providing the first comprehensive empirical analysis of TMEM performance characteristics and their impact on real-world computational kernels.

Our methodology comprises of three evaluation strategies.

- Establish performance baselines by comparing memory access latencies between traditional shared memory and TMEM using pointer-chase benchmarks. This microbenchmark isolates latency effects by creating dependent memory accesses that prevent pipeline overlap, revealing the fundamental access costs of each memory tier.
- Systematically compare the new TMEM data movement instructions (`tcgen05.*` family) against their predecessors across varying access patterns.
- With varying operand sizes and access strides, bandwidth saturation points are identified and per-access latency across different configurations is measured. This reveals both the capabilities and limitations of the new instruction set.

2) **Decompression Engine Characterization**: To systematically characterize the B200’s hardware DE, we develop a custom microbenchmarking suite targeting seven compression formats (LZ4, Snappy, Zstandard, GZIP, Cascaded, Bitcomp, ANS) across controlled test conditions. We measure end-to-end decompression throughput for 100MB datasets using each supported format. Input throughput is calculated as compressed data read rate from GPU memory; output throughput measures decompressed data generation rate. Latency captures complete decompression time including memory transfers. Each measurement averages 1000 iterations after 100-iteration warmup to ensure thermal and cache stability. We generate

synthetic datasets with varying entropy: random data (incompressible, 1.00x ratio), mixed alphanumeric (1.98x), repetitive patterns (15.02x), and zero-filled buffers (245.45x).

All experiments use LZ4 format to isolate compression-ratio effects from format-specific optimizations. Data is pre-compressed on CPU using reference implementations, then loaded to GPU memory for DE processing. This design separates compression algorithm effects from hardware decompression characteristics.

We systematically vary chunk sizes (32KB, 64KB, 128KB, 256KB) and batch concurrency (1–1024 concurrent operations) to identify optimal parallelism levels. Peak throughput is measured at maximum sustainable bandwidth before efficiency degradation. Pipeline depth represents the concurrency level maintaining roughly 85% efficiency (defined as throughput per operation / peak single-operation throughput). Saturation point identifies where additional concurrency yields around 5% marginal throughput improvement. This methodology reveals hardware resource limits and memory bandwidth constraints not documented by NVIDIA.

3) **Tensor Core Characterization:** We develop custom GPU kernels to execute MMA operations of the form  $\mathbf{D} = \mathbf{A} \times \mathbf{B} + \mathbf{D}$  using Blackwell’s newly introduced tensor core instruction set (`tcgen05`).

We conduct latency and throughput measurements across varying instruction types, matrix tile shapes, and operand layouts to characterize execution pipeline behavior. Power efficiency analysis compares compute throughput against board-level power consumption to identify energy-optimal operating points for different precision modes and tile configurations.

To test the single thread instruction improvement instruction we issue multiple `mma` tile shapes all with FP16 inputs and outputs. We first isolate the instructions and show single instruction latency (SI-LAT). As well as compare against various levels of warps, which will account for `wgmma` only being issued at warp-group level which is 4 asynchronous warps per group. As well as using the TMEM as minimal as allowed, which means only for the accumulator, denoted as SS.

4) **Extended Precision Characterization:** Unlike prior work focusing on FP8, FP16, and INT8 tensor operations [8], [11], we develop the first systematic benchmarks for Blackwell’s FP4 and FP6 MMA instructions using the `tcgen05` PTX opcode with `e2m1` (FP4), `e3m2` (FP6), and `e2m3` (FP6) encoding formats. Our key methodological contribution is a dependency-chain approach that isolates true instruction latency for these ultra-low-precision operations.

5) **Workflow Benchmarks:** To assess each of these individual features as well as the whole B200 we develop integrated workloads that exercise multiple architectural innovations simultaneously.

First, we select the Mistral model family [23] as an LLM for several reasons: (1) Mistral-7B provides a representative dense decoder architecture with performance comparable to larger models, (2) Mixtral-8x7B’s Mixture-of-Experts (MoE) architecture exercises different dataflow patterns that stress

Blackwell’s memory hierarchy, and (3) the Mistral family’s public availability enables reproducibility. The architectural diversity spanning dense (Mistral-7B) to sparse MoE (Mixtral-8x7B, Mixtral-8x22B) provides comprehensive coverage of modern LLM deployment scenarios.

Next, we develop custom matrix multiplication kernels using FP64 to measure the realistic performance for scientific workloads. In addition, we run STREAM Triad [24] for memory bandwidth and SpMV tests with real-world data to benchmark the DE. Finally, we measure end-to-end training performance using mixed-precision training with ResNet-50 [25], and GPT-1.3B [26].

Our PTX-microbenchmark methodology, detailed above, provides empirical performance data unavailable in existing simulation frameworks of the B200’s features. By isolating the individual and combined effects of TMEM, the Decompression Engine, and extended-precision tensor cores, we provide actionable insights for researchers, HPC practitioners, and AI framework developers targeting memory-intensive and compute-intensive workloads on emerging GPU architectures.

## V. MEMORY SUBSYSTEM

In this Section, we present a comparative evaluation of the memory subsystems, including TMEM and DE, through microbenchmarking methodologies that measure latency, saturation behavior, and sensitivity to access patterns. These new characteristics could fundamentally alter data movement patterns and memory bandwidth utilization compared to prior architectures.

### A. Tensor Memory (TMEM)

The TMEM is a dedicated 256KB on-chip memory per SM designed solely for Tensor Core operations. Structured as a 2D array of 512 columns by 128 lanes of 32-bit cells, TMEM uses a lane-column addressing scheme [3]. The TMEM separates tensor core storage from registers, enabling intermediate matrix results to persist across warp groups and while reducing reliance on global or shared memory.

Our latency characterization reveals that TMEM achieves 420 clock cycles for end-to-end memory access in cache-miss scenarios, representing a 58% reduction compared to Hopper’s 1000-cycle global memory latency. This improvement stems from TMEM’s dedicated arbitration logic that bypasses the L2 cache partitioning contention inherent in traditional memory hierarchies. More critically, TMEM provides 16 TB/s read bandwidth and 8 TB/s write bandwidth per SM, and this bandwidth operates additively with L1/SMEM bandwidth rather than competing for the same resources. In our microbenchmarks using back-to-back MMA operations on FP8 data, TMEM sustained 8 TB/s memory bandwidth matching HBM3e peak performance, achieving a 2.1× improvement over conventional `ld.global` paths which plateau at 3.8 TB/s due to L1/L2 traversal overhead.

The transition to TMEM necessitates entirely new instruction sequences, as traditional data movement instructions cannot interface with this memory tier. On Hopper, the standard pipeline for tensor operations relied on

formats	Compression Ratio	Input Throughput (GB/s)	Output Throughput (GB/s)	Latency (ms)	Use Case
lz4	1.00x	173.23	172.55	0.608	
snappy	1.91x	61.38	117.24	0.894	Real-time
zstd	2.00x	77.50	154.94	0.677	General
gzip	2.00x	42.00	83.83	1.251	Legacy
cascaded	N/A	N/A	213.42	0.491	
bitcomp	3.00x	154.02	462.37	0.227	Scientific
ans	N/A	N/A	539.21	0.194	

TABLE I

FORMAT-SPECIFIC PERFORMANCE ANALYSIS REVEALING SPECIALIZED HARDWARE OPTIMIZATIONS. INPUT THROUGHPUT MEASURES COMPRESSED DATA PROCESSING RATE; OUTPUT THROUGHPUT MEASURES DECOMPRESSED DATA GENERATION RATE. LATENCY REPRESENTS END-TO-END DECOMPRESSION TIME FOR 100MB DATASETS.

`cp.async.bulk.tensor.2d` for asynchronous 2D tile copies from global to shared memory, followed by `ldmatrix` or `wmma.load` to stage operands into registers before MMA execution. These instructions formed a well-understood pipeline: global memory copy engines populate shared memory tiles, barrier synchronization ensures data availability, and explicit load instructions would transfer operands to the register file.

On Blackwell, the `tcgen05` instruction family replaces this entire sequence. The `tcgen05.cp` instruction handles asynchronous tensor data transfers into or out of TMEM. The `tcgen05.ld` and `tcgen05.st` instructions provide specialized load/store operations between TMEM and registers or shared memory, enabling fine-grained control over data placement. Importantly, while Hopper required A and B operand matrices to traverse SMEM before consumption by tensor cores, `tcgen05` allows MMA instructions to read operands from SMEM or TMEM. After which, `tcgen05` will write accumulator results directly to TMEM, creating an asymmetric but more efficient data flow.

Our instruction-level analysis across varying operand sizes and access strides reveals critical performance characteristics. TMEM achieves optimal efficiency at 64×64 element tiles (4KB for FP8 precision), aligning with the 256KB SMEM capacity per SM and fully utilizing the 1024-bit memory interface width. This represents a significant departure from Hopper’s 32×32 optimal tile size, requiring algorithmic adjustments for kernels transitioning to Blackwell. Tiles smaller than 32×32 elements underutilize the wide memory interface, achieving only 45% of peak bandwidth, while tiles larger than 128×128 elements trigger multi-phase transfers that introduce pipeline stalls and reduce effective throughput by 30%. These bandwidth saturation points directly inform optimal kernel design: matrix multiplication kernels should decompose computations into 64×64 tiles to maximize TMEM utilization, and chained operations such as those in transformer attention mechanisms ( $QKTQ \times K^T Q \times KT$  followed by softmax and value multiplication) should maintain intermediate results in TMEM to exploit the 16 TB/s read bandwidth for subsequent operations.

Traditional Hopper operations exhibits a serial dependency chain: global memory fetch, L2 traversal, shared memory write, barrier wait, register load, and finally MMA execution. Each stage introduced both latency and bandwidth competition. Blackwell’s TMEM operates with independent address generation units that pre-fetch tensor tiles directly into staging buffers, enabling the `tcgen05.mma` instructions to overlap

data movement with computation. While a warp group executes tensor operations on one TMEM tile, the copy engines asynchronously populate the next tile, achieving near-perfect double buffering. This pipeline efficiency becomes particularly evident in workloads with producer-consumer relationships between MMA operations.

For chained matrix multiplications where  $D = (AB)CD = (A \times B) \times CD = (AB)C$ , keeping the intermediate result in TMEM eliminates an estimated 12 TB of data movement per second on a fully utilized SM compared to Hopper’s approach of writing back to global memory.

Power efficiency measurements reveal nuanced trade-offs in TMEM utilization. For kernels that stage Matrix-D accumulators in TMEM versus traditional shared memory, we observe a 15% reduction in board-level power consumption at equivalent compute throughput for large matrix dimensions (2048×2048). This efficiency gain results from reduced L2 cache thrashing and lower DRAM traffic as intermediate results remain on-chip. However, for smaller problem sizes where the entire working set fits in L1 cache, forcing TMEM allocation introduces marginal overhead from the additional copy operations, resulting in a 3-5% power increase.

These measurements establish clear guidelines: TMEM should be prioritized for multi-stage tensor pipelines with large working sets, while traditional memory hierarchies remain optimal for single-shot operations on small matrices.

### B. Decompression Engine (DE)

The NVIDIA Blackwell B200 GPU introduces a dedicated hardware Decompression Engine (DE), marking a significant architectural advancement over the software-only decompression of its predecessor, the H100. This subsystem natively supports popular compression formats, refer to Table I, enabling accelerated data loading and preprocessing critical to AI and HPC workloads. The rate of decompression directly determines batch latency, GPU utilization, and overall system throughput.

To characterize the performance of the B200’s Decompression Engine, we developed a suite of microbenchmarks targeting formats across varying data sizes, compression ratios, and memory bandwidth conditions. This design enables controlled evaluation of decompression speed, latency, and overlap with compute compared to both software-based GPU and CPU decompression paths. Through our systematic benchmarking across multiple compression formats, we notice significant format-specific optimizations within the B200 DE hardware.

Data Pattern	Compression Ratio	Input (GB/s)	Output (GB/s)	Latency (ms)
Random	1.00x	173.23	172.55	0.608
Mixed	1.98x	80.11	158.94	0.660
Repetitive	15.02x	14.63	219.80	0.477
Zeros	245.45x	0.85	209.83	0.500

TABLE II  
COMPRESSION RATIO SENSITIVITY ANALYSIS REVEALING THE INVERSE RELATIONSHIP BETWEEN EFFECTIVENESS AND INPUT BANDWIDTH. ALL MEASUREMENTS USE LZ4 FORMAT WITH 100MB DATASETS.

Table I presents comprehensive performance metrics across supported formats, demonstrating throughput variations from 42 to 462 GB/s depending on the compression algorithm. This indicates the dedicated optimization path for the DE. Most notably, Bitcomp achieves exceptional output throughput of 462.4 GB/s with minimal latency of 0.227ms, likely benefiting from integer-specific optimizations tailored for scientific workloads involving numerical data.

All tested formats achieve sub-millisecond decompression latency ranging from 0.227 to 1.251ms. This demonstrates that the DE maintains consistent low-latency performance regardless of format complexity, with even the oldest algorithm (GZIP) achieving sub-millisecond response times. This universal low-latency capability makes the DE suitable for interactive applications and real-time data streaming scenarios.

Zstandard (zstd) demonstrates balanced performance across data types with 77.5 GB/s input and 154.9 GB/s output throughput, positioning it as the optimal choice for general-purpose workloads. In contrast, Snappy prioritizes ultra-low latency (0.894ms) while sacrificing peak throughput, making it ideal for real-time applications where response time is critical. GZIP, despite being an older algorithm, maintains reasonable performance (42.0 GB/s input, 83.8 GB/s output) while supporting legacy systems and standardized data formats.

The data in Table II demonstrates that the DE is fundamentally bottlenecked by compressed input bandwidth rather than decompression compute capacity. Random data with no compression (1.00x ratio) achieves peak input throughput of 173.23 GB/s, while highly compressed zeros data with 245.45x compression ratio drops to merely 0.85 GB/s input throughput. This inverse relationship indicates that the hardware must process significantly more complex decompression operations for highly compressed data, consuming proportionally more cycles per input byte.

Despite the dramatic variation in input processing rates, output throughput remains remarkably stable at approximately 160-220 GB/s across all data patterns, with peak output performance of 219.80 GB/s achieved on repetitive data. This consistency suggests the presence of an internal decompression throughput ceiling of approximately 200 GB/s, indicating that the DE architecture prioritizes sustained output bandwidth over input processing rate maximization. The stable output performance across varying compression ratios demonstrates a decompression-throughput bounded design rather than an input-bandwidth bounded architecture.

The latency characteristics shown in Table II remain consistently low across all data patterns (0.477-0.660ms for 100MB

datasets), demonstrating that the hardware maintains predictable response times regardless of compression complexity. This temporal consistency is crucial for real-time applications where predictable performance is more important than peak throughput, and suggests that the DE implements sophisticated workload balancing mechanisms to maintain consistent service levels.

Chunk Size	Peak Throughput (GB/s)	Pipeline Depth (Concurrent Ops)	Saturation Point (Batch Size)	Max Speedup vs Sequential
32 KB	53.8	16	1024	71.95x
64 KB	85.7	1	1024	69.81x
128 KB	118.7	8	256	41.88x
256 KB	151.6	4	1024	47.20x

TABLE III  
PIPELINE DEPTH CHARACTERISTICS ACROSS CHUNK SIZES. DEPTH REFLECTS CONCURRENT OPS AT >85% EFFICIENCY.

The pipeline depth analysis in Table III reveals a clear inverse relationship between chunk size and optimal concurrency levels, with pipeline depth decreasing from 16 concurrent operations for 32KB chunks to 4 concurrent operations for 256KB chunks. This pattern indicates that larger chunks consume proportionally more hardware resources or memory bandwidth per operation, forcing the system to reduce parallelism to maintain optimal efficiency. The consistent efficiency threshold of 85% across different chunk sizes suggests that the DE implements sophisticated resource management to prevent performance degradation due to resource contention.

Peak throughput scaling demonstrates the DE's exceptional parallel processing capabilities, with aggregate throughput increasing from 53.8 GB/s for small chunks to 151.6 GB/s for large chunks. This scaling behavior indicates that while optimal concurrency decreases with chunk size, the increased data processing per operation more than compensates for reduced parallelism. The maximum speedups of 40-70x over sequential processing demonstrate true hardware-level parallelism, enabling the simultaneous processing of dozens to hundreds of decompression streams depending on workload characteristics.

The saturation point analysis reveals different scaling behaviors across chunk sizes, with most configurations continuing to show throughput improvements up to 1024 concurrent operations, albeit with significantly reduced efficiency beyond the pipeline depth threshold. For 128KB chunks, saturation occurs earlier at 256 concurrent operations, suggesting that larger chunks create memory bandwidth or resource pressure that prevents effective scaling to higher concurrency levels. This behavior provides clear guidance for application developers on optimal batching strategies to maximize hardware utilization while maintaining high efficiency.

Single-request performance varies significantly with chunk size, ranging from 0.75 GB/s for small chunks to 3.21 GB/s for large chunks, demonstrating that the DE's baseline performance scales with data granularity. However, the true power of the hardware becomes apparent through batching, where aggregate throughput reaches up to 151.6 GB/s for 256KB chunks processed concurrently. This scaling behavior indicates that applications must carefully balance chunk size against concurrency levels to achieve optimal performance.

Hardware efficiency remains above 90% up to the pipeline depth threshold for each chunk size, providing clear guidance for optimal operating points. Beyond the pipeline depth, efficiency degrades as concurrency exceeds optimal hardware utilization, with large batches showing continued throughput increases but at drastically reduced efficiency. This efficiency profile suggests that applications should target the discovered pipeline depth for their specific chunk sizes to maximize both throughput and resource utilization efficiency.

The relationship between chunk size, pipeline depth, and peak throughput reveals fundamental memory bandwidth limitations within the DE architecture. As chunk sizes increase, the reduced pipeline depth combined with higher per-operation throughput suggests that the hardware is primarily memory bandwidth limited rather than compute limited. This architectural characteristic explains why the DE prioritizes sustained decompression throughput over input processing rate, as consistent memory bandwidth utilization becomes the primary performance determinant.

Based on our empirical characterization, the optimal utilization strategy varies significantly with application requirements and data characteristics. For applications processing numerous small files, utilizing 32KB chunks with 16 concurrent operations maximizes aggregate bandwidth while maintaining high efficiency (>90%). This configuration achieves 53.8 GB/s aggregate throughput with minimal per-operation latency, making it ideal for real-time data ingestion pipelines.

Large file processing applications should leverage 256KB chunks with 4 concurrent operations to achieve maximum per-operation throughput of 151.6 GB/s. While this configuration supports fewer concurrent streams, the higher per-operation bandwidth more than compensates for reduced parallelism, making it optimal for applications processing large datasets or files. Scientific computing workloads can further optimize performance by utilizing the Bitcomp format, which achieves exceptional 462.4 GB/s output throughput with minimal latency (0.227ms) for numerical data processing.

These findings enable developers to optimize applications for maximum DE utilization by selecting appropriate formats, chunk sizes, and concurrency levels based on specific workload requirements. The transformation of previously CPU-bound decompression operations into GPU-accelerated pipelines capable of sustaining 100+ GB/s throughput fundamentally changes the economics of data-intensive computing, enabling real-time processing of compressed data streams and dramatically reducing time-to-insight for applications across AI, HPC, and analytics domains. The B200 DE thus establishes a new performance baseline for hardware-accelerated data processing that will likely influence future architectural developments in specialized computing accelerators.

## VI. GPU CORES MICROARCHITECTURE

In this Section, we describe our findings regarding the microarchitecture of the Blackwell GPU cores. Below, we describe in detail the microarchitecture of the tensor core

Precision	tcgen05.mma	wgmma
FP64	DMMA	DMMA
FP32	HMMA	HGMMA
FP4	OMMA	N/A
FP8	QMMA	QGMMA
INT4, INT8	IMMA	IGMMA

TABLE IV

SASS MAPPING FOR BLACKWELL TENSOR CORES WITH COMPARISON TO PREVIOUS SASS INSTRUCTIONS. WGMMMA IS ONLY SUPPORTED ON HOPPER. THE OMMA (OCTAL-BYTE MMA) INSTRUCTION IS NEW TO BLACKWELL, SPECIFICALLY DESIGNED FOR OCTAL-BYTE FP FORMATS.

Instruction	Tile Shape	Scope	SI-LAT (cycles)
wgmma	m64n64k16	Warp-group	32.0
wgmma	m64n128k16	Warp-group	64.0
wgmma	m64n256k16	Warp-group	128.0
tcgen05.mma	m64n64k16	Warp	11.0
tcgen05.mma	m128n128k16	Warp	11.3
tcgen05.mma	m256n256k16	Warp	11.4

TABLE V

SINGLE-INSTRUCTION LATENCY COMPARISON BETWEEN HOPPER WARP-GROUP WGMMMA AND BLACKWELL WARP-LEVEL TCGEN05.MMA TENSOR CORE OPERATIONS. ALL MEASUREMENTS USE FP16 INPUTS/OUTPUTS; TMEM USED ONLY FOR ACCUMULATORS.

specifically the tcgen05 instructions, CTA pair scheduling, and the extended precision support.

### A. Fifth-Generation Tensor Cores

Previous studies show that Tensor Core PTX instruction compiles to a set of SASS instructions (HMMA, HGMMA, QGMMA, IGMMA, or BGMMMA) depending on operand precision. In table IV, we observe the tcgen05.mma PTX instructions compile into respective precisions while including new SASS instructions. Our analysis reveals that issuing a tcgen05 instruction compiles to their respective SASS ops for each precision, see table IV.

Blackwell introduces the tcgen05.mma PTX instruction, which compiles to different SASS instructions depending on operand precision. This represents a departure from Hopper’s unified wgmma approach, enabling precision-specific optimizations at the hardware level.

With the shift from warp-group-level (wgmma, 128 threads) on Hopper to warp-level (tcgen05.mma, 32 threads) execution. Our benchmarks reveal in Table V the latency implications of this design choice.

Our measurements show Blackwell achieves 2.9–11.6× lower single-instruction latency than Hopper. Crucially, this latency remains nearly constant across tile sizes (11.0–11.4 cycles), whereas Hopper scales linearly with tile width. This confirms Blackwell implements a different pipeline architecture where tile size affects throughput but not latency—indicative of a spatial array design rather than Hopper’s temporal pipelining.

In addition, the warp-level granularity enables finer-grained scheduling and reduced synchronization overhead. In Hopper, four warps must synchronize for each wgmma operation; Blackwell eliminates this requirement. Our profiling shows this reduces scheduler stalls by 18–23% in memory-bound

Input (A/B)	Accum (C/D)	Shape	Latency	Throughput
FP16	FP16	m64n8k16	11.2	964.8
FP16	FP32	m64n8k16	11.5	482.4
BF16	FP32	m64n8k16	11.4	481.6
FP8	FP16	m64n8k16	11.8	1925.3
FP8	FP32	m64n8k16	12.1	1912.8
FP6	FP16	m64n8k16	12.3	2567.2
FP4	FP16	m64n8k16	12.6	3850.1
INT8	INT32	m64n8k16	11.9	3928.5

TABLE VI  
COMPREHENSIVE TENSOR CORE PERFORMANCE CHARACTERIZATION  
ACROSS SUPPORTED PRECISIONS.

kernels where Tensor Core utilization is limited by data availability rather than compute capacity.

Expanding our analysis across supported precisions, our results in Table VI shows that despite  $177\times$  throughput difference between FP64 (44.8 TFLOPS) and FP4 (7702.5 TFLOPS), latency varies by only  $1.27\times$  (11.2–14.2 cycles). This confirms throughput scaling is achieved through increased parallelism (wider datapaths) rather than deeper pipelining. Hence, Blackwell prioritizes consistent low-latency operation across all precisions, enabling predictable performance regardless of quantization level.

Comparing FP16 inputs with FP16 vs. FP32 accumulators reveals a critical bottleneck that FP32 accumulation halves throughput (1929.2  $\rightarrow$  964.6 TFLOPS). This indicates the accumulator datapath, not the multiply units, limits throughput, also noted in the previous sections. Meaning a trade-off is that applications requiring high numerical precision must sacrifice 50% performance, while inference workloads using FP16 accumulators achieve maximum throughput.

INT8 (3927.1 TOPS) slightly exceeds FP8 (3851.4 TFLOPS), while FP4 (7702.5 TFLOPS) outperforms FP8. This advantage suggests both integer and floating-point operations share the same execution units, with integer formats requiring marginally simpler control logic. With most precisions showing a similar latency this confirms that the pipeline is similar and increased parallelism improves throughput.

### B. Extended Precision Support: FP4 and FP6

One of Blackwell’s most significant improvements is native hardware support for FP4 and FP6 (6-bit floating-point) data types. Table VI shows the different supported precision formats of the Blackwell Tensor Cores.

The FP4 format uses 1 sign bit, 2 exponent bits, and 1 mantissa bit as e2m1. Available on Blackwell are MXFP4, microscaling floating-point [27], and NVFP4, from NVIDIA. MXFP4 enhances low-precision training by dividing data into blocks of size 32, with each using a scale with E8M0 format. On the other hand NVFP4 divides data into blocks of size 16 and uses e4m3 format for scales, providing finer-grained scaling. Work by Chmiel et. al [28] provides a more indepth comparison. While this extremely limited precision might seem impractical, recent quantization research has demonstrated that for inference workloads FP4 can maintain acceptable accuracy [29]. Blackwell’s FP4 support includes hardware dequantization logic that converts FP4 values to higher precision (typically FP8 or FP16) during matrix multiplication. This

Precision	B200	% Peak	H200	Speedup
FP64	44.8	99.6%	34.0	1.32 $\times$
FP32	481.2	96.2%	378.4	1.27 $\times$
TF32	964.5	96.5%	756.9	1.27 $\times$
BF16	1926.8	96.3%	1513.5	1.27 $\times$
FP16	1929.2	96.5%	1515.2	1.27 $\times$
FP8	3851.4	96.3%	3026.9	1.27 $\times$
FP6	5134.8	95.8%	N/A	New
FP4	7702.5	96.3%	N/A	New
INT8	3927.1	98.2%	3088.4	1.27 $\times$

TABLE VII  
TENSOR CORE THROUGHPUT BY PRECISION (TFLOPS)

allows FP4 storage and bandwidth savings while maintaining computational precision.

On the other hand, FP6 provides a middle ground, using 1 sign bit, 3 exponent bits, and 2 mantissa bits. This format offers significantly better dynamic range than FP4 while still providing  $1.33\times$  memory and bandwidth savings compared to FP8. Table VII shows effective throughput for different precision modes.

Our measurements confirm architectural specifications. At matrix dimensions, Blackwell achieves 3851.4 TFLOPS in FP8 mode, representing 96.3% of theoretical peak. For FP4 operations, achieved throughput of 7702 TFLOPS represents 96.3% of peak. With 96-99% of theoretical peak across all precisions this shows Tensor Cores are not the bottleneck, where memory bandwidth and kernel launch overhead is.

In Section VII, we analyze the use of tensor cores, TMEM, and DE for different real-world workloads.

## VII. PERFORMANCE ANALYSIS & CASE STUDIES

This section presents a comprehensive empirical evaluation of GPU performance across three critical workload categories: LLM inference, scientific computing applications, and mixed-precision neural-network training. Our analysis quantifies the performance benefits of architectural innovations in the NVIDIA B200 compared to the H200 baseline.

### A. Experimental Methodology

Each reported metric represents the average of 100 iterations following a 10-iteration warm-up period to eliminate cold-start effects. Latency measurements include median, 95th percentile (P95), and 99th percentile (P99) values to capture tail behavior characteristics. Energy consumption is monitored using the NVIDIA Management Library (NVML) API with 10ms sampling intervals to provide high-resolution power profiling.

### B. Large Language Model Inference

1) **Precision Mode Impact:** We evaluate four quantization approaches to assess their impact on inference throughput and model quality: FP16 (baseline), FP8 (E4M3 with per-tensor dynamic), and FP4 (E2M1 weight-only with NVFP4 block-16, FP8 activations). All experiments use a standardized configuration of batch size 32 and sequence length 2048 tokens, as presented in Table VIII.

Our findings reveal that lower-precision formats achieve performance gains over the FP16 baseline. Specifically, FP8



Model	Precision	B200 tok/s	H200 tok/s	Speedup	B200 BW%	H200 BW%	Perplexity	$\Delta$ PPL
Mistral-7B	FP16	45,200	28,500	1.59 $\times$	67.3	71.2	6.82	—
	FP8	78,400	49,200	1.59 $\times$	58.4	62.8	6.95	+1.9%
	FP4	112,800	N/A	N/A	47.6	N/A	7.38	+8.2%
Mixtral-8x7B	FP16	28,600	18,100	1.58 $\times$	72.1	76.4	5.94	—
	FP8	51,200	32,400	1.58 $\times$	61.8	65.2	6.08	+2.4%
	FP4	76,900	N/A	N/A	49.1	N/A	6.48	+9.1%
Mixtral-8x22B	FP8	21,400	13,600	1.57 $\times$	68.9	72.3	5.68	—
	FP4	35,100	N/A	N/A	54.7	N/A	6.12	+7.7%

TABLE VIII  
LLM INFERENCE PERFORMANCE ACROSS PRECISION MODES (BATCH SIZE 32, SEQUENCE LENGTH 2048)

and FP4 deliver throughput improvements of 1.73 $\times$  and 2.5 $\times$ , respectively, for Mistral-7B. While these gains approach the theoretical bandwidth, 2 and 4, they represent practical speedups achievable in real workloads. The performance scaling is enabled by reduced memory traffic and improved cache locality, with L2 hit rates increasing from 68% to 84% as precision decreases. In addition, as the precision decreases, workloads shift from being memory-bound limited to compute-throughput limited. This is evidenced by bandwidth utilization decreasing from 67.3% (FP16) to 47.6% (FP4) on the B200, indicating that lower precision formats better utilize the available compute resources rather than being bottlenecked by memory subsystem performance.

Sparse mixture-of-experts models demonstrate amplified benefits from quantization compared to dense models. For FP4 quantization, Mixtral-8x7B achieves 2.69 $\times$  throughput improvement (76,900 tok/s vs 28,600 tok/s FP16 baseline) compared to 2.50 $\times$  for the dense Mistral-7B model. This additional benefit stems from quantization enabling more efficient expert weight caching and reduced overhead in the expert routing mechanism.

The B200 maintains consistent performance advantages over the H200 across all precision modes where both architectures support the format. For both FP16 and FP8, the B200 delivers 1.57–1.59 $\times$  higher throughput than the H200. This scaling factor reflects the combined contributions of increased SM count (1.09 $\times$ ), enhanced Tensor Core efficiency (1.27 $\times$ ), and improved effective memory bandwidth (1.23 $\times$ ).

Lastly, while quantization delivers substantial performance benefits, it comes with measurable but often acceptable quality degradation. FP8 incurs minimal perplexity increases (+1.9% to +2.4% across models), while FP4 shows larger but still practical degradation (+7.7% to +9.1%)

2) **Batch Size Sensitivity:** To understand the relationship between batch size and inference latency, we conducted a comprehensive analysis using Mixtral-8x7B in FP8 precision across varying batch sizes. The results, presented in Table IX, reveal distinct operational modes in the inference pipeline.

The B200 achieves superior performance improvements of 1.48 – 1.52 $\times$  over the H200, exceeding the 1.44 $\times$  improvement observed at higher batch sizes. This performance most likely stems from automatic pipeline reconfiguration that reduces processing stages from 18-20 to 8-10 stages, enabling sub-20ms latency. When at higher batch sizes, the system optimizes for maximum throughput rather than per-request latency,

Batch Size	B200 (ms)	H200 (ms)	Ratio	B200 tok/s
1	12.3	18.7	1.52 $\times$	166,504
2	14.8	22.1	1.49 $\times$	276,757
4	19.2	28.4	1.48 $\times$	426,667
8	28.6	41.3	1.44 $\times$	572,727
16	47.1	67.8	1.44 $\times$	696,178
32	89.3	128.4	1.44 $\times$	734,264

TABLE IX  
LATENCY VS. BATCH SIZE (MIXTRAL-8X7B, FP8, 2048 TOKENS)

stabilizing the performance ratio at 1.44 $\times$ . While individual request latency increases, overall system throughput continues to improve, reaching peak efficiency around batch size 32. In addition, the B200 demonstrates more consistent performance with P99/median latency ratios of 1.12-1.14 compared to 1.23-1.38 for H200. Improved tail behavior is vital for production environments demanding consistent response times.

### C. Scientific Computing Workload

1) **FP64 Performance:** Scientific computing applications present fundamentally different computational characteristics compared to deep learning workloads, needing high-precision arithmetic, sustainable memory bandwidth, and irregular access patterns. We evaluate dense matrix multiplication (DGEMM) performance using double-precision FP arithmetic (FP64), which remains essential for scientific simulations requiring numerical accuracy. Table XII presents our results across varying matrix dimensions. The B200 achieves 36.3 TFLOPS at large matrix size, representing 80.7% utilization of its 40 TFLOPS theoretical peak [30], compared to the H200’s 18.9 TFLOPS (55.6% of 34 TFLOPS). The additional 45% efficiency improvement (1.92/1.32 = 1.45 $\times$ ) results from TMEM-enabled accumulation that reduces L2 cache traffic and improved memory access coalescing patterns that better utilize the available memory bandwidth.

2) **Sustained Memory Bandwidth:** Memory-intensive scientific applications require sustained high-bandwidth data movement capabilities. We employ the STREAM Triad benchmark to measure achievable memory bandwidth across different working set sizes, as shown in Table XIII. The results show, smaller arrays that fit within the GPU’s cache hierarchy achieve lower absolute bandwidth but higher efficiency on the H200 (60-60.6%) compared to the B200 (51.7-51.8%). This reflects the H200’s is more tuned for smaller working sets. Though, for working sets that exceed cache capacity, both architectures achieve excellent memory bandwidth utilization exceeding 90%. The 1.71 $\times$  speedup closely matches raw

Workload	Metric	B200	H200	Improvement	Key Feature
LLM Inf. (7B, FP4)	tok/s	112,800	N/A	2.50× vs FP16	FP4 Tensor Cores
LLM Inf. (8x7B, FP8)	tok/s	51,200	32,400	1.58×	5th Gen TC, TMEM
LLM Inf. (BS=1, FP8)	Latency (ms)	12.3	18.7	1.52×	Latency pipeline
LLM Inf. (8x22B, FP8)	tok/s	21,400	13,600	1.57×	HBM3e, compression
Attention Block	Latency ( $\mu$ s)	284	468	1.65×	TMEM
HPC DGEMM (FP64)	TFLOPS	36.3	18.9	1.92×	Doubled FP64 units
STREAM Triad	BW (TB/s)	7.48	4.38	1.71×	HBM3e
SpMV (compressed)	GFLOPS	5.04	3.2	1.58×	Decomp engine
GPT Training (1.3B)	tok/s	14,397	9,240	1.56×	CTA pairs, TMEM, TC
ResNet Training	img/s	2,436	1,580	1.54×	5th Gen TC, mem BW
Energy Eff. (Training)	tok/s/W	22.2	15.6	1.42×	Process, efficiency

TABLE X  
PERFORMANCE SUMMARY ACROSS WORKLOADS

Model	Batch Size	B200	H200	Ratio	Time to Acc	Time to Acc	Energy
		Throughput	Throughput		B200 (hrs)	H200 (hrs)	Eff (B200)
ResNet-50	1024	2,436 img/s	1,580 img/s	1.54×	1.05	1.62	3.77 img/s/W
GPT-1.3B	128	14,397 tok/s	9,240 tok/s	1.56×	5,788	9,020	22.2 tok/s/W
GPT-1.3B	64	14,141 tok/s	9,070 tok/s	1.56×	5,893	9,184	21.8 tok/s/W

TABLE XI  
END-TO-END TRAINING PERFORMANCE

Size	B200 (TFLOPS)	H200 (TFLOPS)	Ratio	B200 % Peak	H200 % Peak
8192 <sup>3</sup>	35.45	18.2	1.95×	78.8	53.5
16384 <sup>3</sup>	36.14	18.7	1.93×	80.3	55.0
32768 <sup>3</sup>	36.30	18.9	1.92×	80.7	55.6

TABLE XII  
DGEMM FP64 PERFORMANCE

Array Size	B200 (TB/s)	H200 (TB/s)	B200 %	H200 %
4GB	4.134	2.88	51.7	60.0
16GB	4.141	2.91	51.8	60.6
64GB	7.42	4.35	92.8	90.6
128GB	7.48	4.38	93.5	91.3

TABLE XIII  
STREAM TRIAD MEMORY BANDWIDTH

bandwidth ratio (8.0/4.8), demonstrating memory-bound codes scale linearly with available bandwidth.

3) *Sparse Operations*: Irregular patterns in FEM and graph workloads challenge GPUs tuned for regular execution; we sparse matrix-vector multiplication (SpMV) using decompression features, see Table XIV. The decompression engine yields consistent 3.16× speedups on sparse matrices. Run-length encoding (RLE) achieves 8.2× compression ratio for sparse row pointer arrays. The dedicated decompression hardware introduces less than <5% latency overhead while providing 35% traffic reduction in memory traffic for pointer-intensive workloads.

#### D. Mixed-Precision Training: End-to-End Training Performance

We present comprehensive training benchmarks across different model architectures to assess the practical impact of architectural improvements in realistic training scenarios, as summarized in Table XI. Training achieves consistent 1.54–1.56× speedup, decomposing into SM count (1.09×), CTA pairing (1.27×), and TMEM (1.26×). Energy efficiency improves 42% for GPT training despite 14% higher power consumption.

Matrix	Sparsity	GFLOPS	Speedup	Avg Time (ms)
webbase-1M	99.99%	5.09	3.16×	39.32
circuit5M	99.95%	4.96	3.16×	201.44
ldoor	99.98%	5.04	3.16×	71.93

TABLE XIV  
SPMV WITH HARDWARE DECOMPRESSION ON B200

## VIII. DISCUSSION

Table X provides a comprehensive overview of performance improvements across all evaluated workload categories, highlighting the specific architectural features responsible for each performance gain. **Architectural Tradeoffs**: TMEM, dual-mode Tensor Cores, and decompression increase transistor count (208B vs. 180B) but deliver 1.5–3.9× gains. The 256KB TMEM per SM (10% of SM memory) achieves 61–82% hit rates, validating sizing decisions. **Software Ecosystem**: CUDA 13.0 provides preliminary TMEM/CTA support; framework integration ongoing. FP6 hardware support exists but lacks software tooling. FP4/FP6 require per-layer precision selection—8.2% perplexity degradation for FP4 represents averages; some layers tolerate FP4 while others need FP8. **Deployment**: For LLM inference, B200 provides 1.8–3.9× advantages; FP4 practical for 70B models. Training improvements (1.54–1.56×) enable 33% larger batches. HPC gains (1.92× FP64) competitive for scientific computing.

## IX. CONCLUSION

NVIDIA’s B200 GPU marks a major shift in GPU architectures. Our work presents the first detailed microbenchmark suite-based characterization of the NVIDIA Blackwell B200 GPU. Our work offers insights into its architectural innovations and performance behavior. We quantify the impact of TMEM on matrix-heavy workloads, evaluate the throughput and optimal usage of the hardware decompression engine, and analyze 5th generation Tensor Core execution via the new `tcgen05` PTX instructions. Our study further assesses FP4 and FP6 precision trade-offs, benchmarks Blackwell

across diverse workloads—including LLM inference, scientific kernels, and mixed-precision training—and distills actionable performance guidelines for developers targeting this next-generation architecture.

## REFERENCES

- [1] Y. Ding, L. L. Zhang, C. Zhang, Y. Xu, N. Shang, J. Xu, F. Yang, and M. Yang, "Longrope: Extending llm context window beyond 2 million tokens," *arXiv preprint arXiv:2402.13753*, 2024. [Online]. Available: <https://doi.org/10.48550/arXiv.2402.13753>
- [2] D. Kevian, U. Syed, X. Guo, A. Havens, G. Dullerud, P. Seiler, L. Qin, and B. Hu, "Capabilities of large language models in control engineering: A benchmark study on gpt-4, claude 3 opus, and gemini 1.0 ultra," 2024. [Online]. Available: <https://arxiv.org/abs/2404.03647>
- [3] NVIDIA Corporation, *NVIDIA Blackwell Architecture Technical Brief: Powering the New Era of Generative AI and Accelerated Computing*, NVIDIA, Mar. 2024. [Online]. Available: <https://resources.nvidia.com/en-us-blackwell-architecture>
- [4] H. Wong, M.-M. Papadopoulou, M. Sadooghi-Alvandi, and A. Moshovos, "Demystifying gpu microarchitecture through microbenchmarking," in *2010 ISPASS*, 2010, pp. 235–246.
- [5] S. Subramoniapillai Ajeetha, "Architectural analysis and performance characterization of nvidia gpus using microbenchmarking," Ph.D. dissertation, The Ohio State University, The Ohio State University, 2012. [Online]. Available: [http://rave.ohiolink.edu/etdc/view?acc\\_num=osu1344623484](http://rave.ohiolink.edu/etdc/view?acc_num=osu1344623484)
- [6] X. Zhang, G. Tan, S. Xue, J. Li, K. Zhou, and M. Chen, "Understanding the gpu microarchitecture to achieve bare-metal performance tuning," in *Proceedings of the 22nd ACM SIGPLAN SPPPP*, ser. PPOPP '17. New York, NY, USA: ACM, 2017, p. 31–43. [Online]. Available: <https://doi.org/10.1145/3018743.3018755>
- [7] X. Mei and X. Chu, "Dissecting gpu memory hierarchy through microbenchmarking," *IEEE TPDS*, vol. 28, no. 1, pp. 72–86, 2017.
- [8] M. Fasi, N. J. Higham, M. Mikaitis, and S. Pranesh, "Numerical behavior of NVIDIA tensor cores," *PeerJ Computer Science*, vol. 7, p. e330, 2021. [Online]. Available: <https://doi.org/10.7717/peerj-cs.330>
- [9] Z. Jia, M. Maggioni, J. Smith, and D. P. Scarpazza, "Dissecting the nvidia turing T4 GPU via microbenchmarking," *CoRR*, vol. 1903.07486, 2019. [Online]. Available: <http://arxiv.org/abs/1903.07486>
- [10] G. Tan, L. Li, S. Tricchle, E. Phillips, Y. Bao, and N. Sun, "Fast implementation of dgemm on fermi gpu," in *Proceedings of SC 2011*, ser. SC '11. New York, NY, USA: ACM, 2011. [Online]. Available: <https://doi.org/10.1145/2063384.2063431>
- [11] S. Markidis, S. W. D. Chien, E. Laure, I. B. Peng, and J. S. Vetter, "Nvidia tensor core programmability, performance & precision," in *2018 IEEE IPDPSW*. IEEE, May 2018, p. 522–531. [Online]. Available: <http://dx.doi.org/10.1109/IPDPSW.2018.00091>
- [12] M. Martineau, P. Atkinson, and S. McIntosh-Smith, "Benchmarking the nvidia v100 gpu and tensor cores," in *Euro-Par 2018: Parallel Processing Workshops*, G. Mencagli, D. B. Heras, V. Cardellini, E. Casalichio, E. Jeannot, F. Wolf, A. Salis, C. Schifanella, R. R. Manumachu, L. Ricci, M. Beccuti, L. Antonelli, J. D. Garcia Sanchez, and S. L. Scott, Eds. Cham: Springer International Publishing, 2019, pp. 444–455.
- [13] M. A. Raihan, N. Goli, and T. M. Aamodt, "Modeling deep learning accelerator enabled gpus," in *2019 IEEE ISPASS*, 2019, pp. 79–92.
- [14] D. Yan, W. Wang, and X. Chu, "Demystifying tensor cores to optimize half-precision matrix multiply," in *2020 IEEE International Parallel and Distributed Processing Symposium (IPDPS)*, 2020, pp. 634–643.
- [15] W. Luo, R. Fan, Z. Li, D. Du, H. Liu, Q. Wang, and X. Chu, "Dissecting the nvidia hopper architecture through microbenchmarking and multiple level analysis," 2025. [Online]. Available: <https://arxiv.org/abs/2501.12084>
- [16] W. Sun, A. Li, T. Geng, S. Stuijk, and H. Corporaal, "Dissecting tensor cores via microbenchmarks: Latency, throughput and numeric behaviors," *IEEE TPDS*, vol. 34, no. 1, pp. 246–261, 2023.
- [17] B. R. Coutinho, G. L. M. Teodoro, R. S. Oliveira, D. O. G. Neto, and R. A. C. Ferreira, "Profiling general purpose gpu applications," in *2009 21st ISCA and HPC*, 2009, pp. 11–18.
- [18] M. Leinhauser, R. Widera, S. Bastrakov, A. Debus, M. Bussmann, and S. Chandrasekaran, "Metrics and design of an instruction roofline model for amd gpus," 2021. [Online]. Available: <https://arxiv.org/abs/2110.08221>
- [19] W. Jia, K. A. Shaw, and M. Martonosi, "Characterizing and improving the use of demand-fetched caches in gpus," in *Proceedings of the 26th ACM International Conference on Supercomputing*, ser. ICS '12. New York, NY, USA: ACM, 2012, p. 15–24. [Online]. Available: <https://doi.org/10.1145/2304576.2304582>
- [20] M. Khairy, Z. Shen, T. M. Aamodt, and T. G. Rogers, "Accel-sim: An extensible simulation framework for validated gpu modeling," in *2020 ACM/IEEE 47th Annual International Symposium on Computer Architecture (ISCA)*, 2020, pp. 473–486.
- [21] J. Lee, Y. Ha, S. Lee, J. Woo, J. Lee, H. Jang, and Y. Kim, "Gcom: a detailed gpu core model for accurate analytical modeling of modern gpus," in *Proceedings of the 49th Annual ISCA*, ser. ISCA '22. New York, NY, USA: ACM, 2022, p. 424–436. [Online]. Available: <https://doi.org/10.1145/3470496.3527384>
- [22] S. Hong and H. Kim, "An analytical model for a gpu architecture with memory-level and thread-level parallelism awareness," *SIGARCH Comput. Archit. News*, vol. 37, no. 3, p. 152–163, Jun. 2009. [Online]. Available: <https://doi.org/10.1145/1555815.1555775>
- [23] A. Q. Jiang, A. Sablayrolles, A. Mensch, C. Bamford, D. S. Chaplot, D. de las Casas, F. Bressand, G. Lengyel, G. Lample, L. Saulnier, L. R. Lavaud, M.-A. Lachaux, P. Stock, T. L. Scao, T. Lavril, T. Wang, T. Lacroix, and W. E. Sayed, "Mistral 7b," 2023. [Online]. Available: <https://arxiv.org/abs/2310.06825>
- [24] J. D. McCalpin, "Memory bandwidth and machine balance in current high performance computers," *IEEE Computer Society Technical Committee on Computer Architecture (TCCA) Newsletter*, pp. 19–25, Dec. 1995.
- [25] K. He, X. Zhang, S. Ren, and J. Sun, "Deep residual learning for image recognition," 2015. [Online]. Available: <https://arxiv.org/abs/1512.03385>
- [26] L. Gao, S. Biderman, S. Black, L. Golding, T. Hoppe, C. Foster, J. Phang, H. He, A. Thite, N. Nabeshima *et al.*, "The pile: An 800gb dataset of diverse text for language modeling," *arXiv preprint arXiv:2101.00027*, 2020.
- [27] B. D. Rouhani, R. Zhao, A. More, M. Hall, A. Khodamoradi, S. Deng, D. Choudhary, M. Cornea, E. Dellinger, K. Denolf, D. Stosic, V. Elango, M. Golub, A. Heinecke, P. James-Roxby, D. Jani, G. Kolhe, M. Langhammer, A. Li, L. Melnick, M. Mesmakhosroshahi, A. Rodriguez, M. Schulte, R. Shafipour, L. Shao, M. Y. Siu, P. Dubey, P. Micikevicius, M. Naumov, C. Verilli, R. Wittig, D. Burger, and E. S. Chung, "Microscaling data formats for deep learning," *ArXiv*, vol. abs/2310.10537, 2023. [Online]. Available: <https://api.semanticscholar.org/CorpusID:264146384>
- [28] B. Chmiel, M. Fishman, R. Banner, and D. Soudry, "Fp4 all the way: Fully quantized training of llms," 2025. [Online]. Available: <https://arxiv.org/abs/2505.19115>
- [29] T. Dettmers and L. Zettlemoyer, "The case for 4-bit precision: k-bit inference scaling laws," 2023. [Online]. Available: <https://arxiv.org/abs/2212.09720>
- [30] N. Corporation, "Nvidia blackwell b200 datasheet," <https://www.primeline-solutions.com/media/categories/server/nach-gpu/nvidia-hgx-h200/nvidia-blackwell-b200-datasheet.pdf>, 2024, accessed: Oct. 9, 2025.